

See discussions, stats, and author profiles for this publication at: <https://www.researchgate.net/publication/254999173>

# New Insights into the Crystal and Electronic Structures of Li<sub>1+x</sub>V<sub>1-x</sub>O<sub>2</sub> from Solid State NMR, Pair Distribution Function Analyses, and First Principles Calculations

ARTICLE *in* CHEMISTRY OF MATERIALS · AUGUST 2012

Impact Factor: 8.35 · DOI: 10.1021/cm300662m

---

CITATIONS

8

---

READS

30

## 6 AUTHORS, INCLUDING:



Xiao Hua

Université de Fribourg

6 PUBLICATIONS 223 CITATIONS

[SEE PROFILE](#)



Clare P Grey

University of Cambridge

428 PUBLICATIONS 11,321 CITATIONS

[SEE PROFILE](#)

# New Insights into the Crystal and Electronic Structures of $\text{Li}_{1+x}\text{V}_{1-x}\text{O}_2$ from Solid State NMR, Pair Distribution Function Analyses, and First Principles Calculations

Frédérique Pourpoint,<sup>†,‡</sup> Xiao Hua,<sup>†,‡</sup> Derek S. Middlemiss,<sup>†</sup> Paul Adamson,<sup>‡</sup> Da Wang,<sup>‡</sup> Peter G. Bruce,<sup>‡</sup> and Clare P. Grey\*,<sup>†,§</sup>

<sup>†</sup>Department of Chemistry, University of Cambridge, Lensfield Road, Cambridge, CB2 1EW, United Kingdom

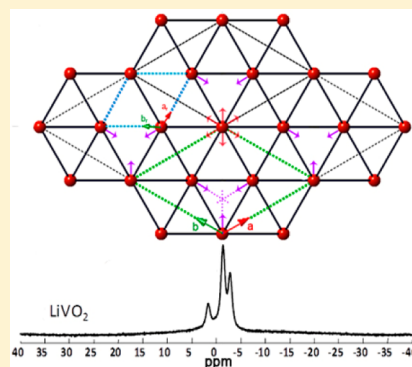
<sup>‡</sup>School of Chemistry, University of St. Andrews, North Haugh, St. Andrews, Fife, KY16 9ST, United Kingdom

<sup>§</sup>Department of Chemistry, Stony Brook University, Stony Brook, New York 11794-3400, United States

## Supporting Information

**ABSTRACT:** Pair distribution function (PDF) analyses of synchrotron data obtained for the anode materials  $\text{Li}_{1+x}\text{V}_{1-x}\text{O}_2$  ( $0 \leq x \leq 0.1$ ) have been performed to characterize the short to medium range structural ordering. The data show clear evidence for the magnetically-induced distortion of the V sublattice to form trimers, the distortion persisting at even the highest excess Li content considered of  $x = 0.1$ . At least three distinct local environments were observed for the stoichiometric material  $\text{LiVO}_2$  in  ${}^6\text{Li}$  nuclear magnetic resonance (NMR) spectroscopy, the environments becoming progressively more disordered as the Li content increases. A two-dimensional Li–Li correlation NMR experiment (POST-C7) was used to identify the resonances corresponding to Li within the same layers. NMR spectra were acquired as a function of the state of charge, a distinct environment for Li in  $\text{Li}_2\text{VO}_2$  being observed. The results suggest that disorder within the Li layers (in addition to the presence of Li within the V layers as proposed by Armstrong et al. *Nat. Mater.* **2011**, *10*, 223–229) may aid the insertion of Li into the  $\text{Li}_{1+x}\text{V}_{1-x}\text{O}_2$  phase. The previously little-studied  $\text{Li}_2\text{VO}_2$  phase was also investigated by hybrid density functional theory (DFT) calculations, providing insights into magnetic interactions, spin–lattice coupling, and Li hyperfine parameters.

**KEYWORDS:**  $\text{LiVO}_2$ , PDF analyses,  ${}^6\text{Li}$  NMR, first principles calculations, POST-C7, trimer, spin–lattice interaction



## 1. INTRODUCTION

Layered oxide materials such as  $\text{LiCoO}_2$ ,  $\text{LiNiO}_2$ , and  $\text{LiVO}_2$  and their substituted variants have been widely studied as potential insertion electrodes for lithium-ion batteries.<sup>1–4</sup> Among this diversity of layered materials,  $\text{Li}_{1+x}\text{V}_{1-x}\text{O}_2$  stands out for the reason that it intercalates Li at very low voltage and may thus find use as a practical anode material.<sup>5,6</sup> A previous study has shown that the Li-excess material  $\text{Li}_{1.07}\text{V}_{0.93}\text{O}_2$  exhibits much better electrochemical performance than the stoichiometric material  $\text{LiVO}_2$ , which does not readily insert additional Li. Neutron diffraction studies of electrochemically lithiated  $\text{Li}_{1.07}\text{V}_{0.93}\text{O}_2$  phases have demonstrated the presence of an intermediate phase, followed by a two phase reaction leading to  $\text{Li}_2\text{VO}_2$ .<sup>7</sup>

Stoichiometric  $\text{LiVO}_2$  crystallizes in an ordered rocksalt-related  $R\bar{3}m$  structure with  $\text{Li}^+$  and  $\text{V}^{3+}$  occupying alternating (111) planes (Figure 1). The material has been the subject of numerous previous investigations primarily on the basis of its magnetic properties,<sup>8,9</sup> the presence of a two-dimensional (2D) triangular lattice of  $\text{V}^{3+}$   $3d^2$  ions together with antiferromagnetic exchange coupling leading to geometrical frustration.<sup>10</sup> The frustration is partially alleviated by the formation of

clusters composed of singlet  $\text{V}^{3+}$ – $\text{V}^{3+}$ – $\text{V}^{3+}$  trimers at ambient temperature, the V ions experiencing small coplanar shifts from their ideal positions toward the center of a mutually defined triangle, as illustrated schematically in Figure 1. The spin–singlet trimerization is driven by orbital ordering and polarization involving the three  $\text{V}^{3+}$   $t_{2g}(\uparrow\uparrow)$  manifolds in each triangular unit.<sup>11–13</sup> A superlattice structure results, characterized by a (1/3 1/3 0) reflection (with indexing based upon the original  $\alpha\text{-NaFeO}_2$  type cell) observed by X-ray<sup>10,13</sup> and electron<sup>11</sup> diffraction. On heating, a first order phase transition is observed accompanied by considerable hysteresis (the critical temperature,  $T_c$ , is  $\sim 500$  K on heating and  $\sim 400$  K on cooling). This material is essentially diamagnetic below  $T_c$ , behaving as a Curie–Weiss paramagnet above this temperature.<sup>14–16</sup>

Pair distribution function (PDF) analysis, magic angle spinning nuclear magnetic resonance (MAS NMR) spectroscopy, and first principles solid state density functional theory (DFT) calculations constitute an effective set of mutually

Received: February 29, 2012

Revised: June 19, 2012

Published: June 25, 2012



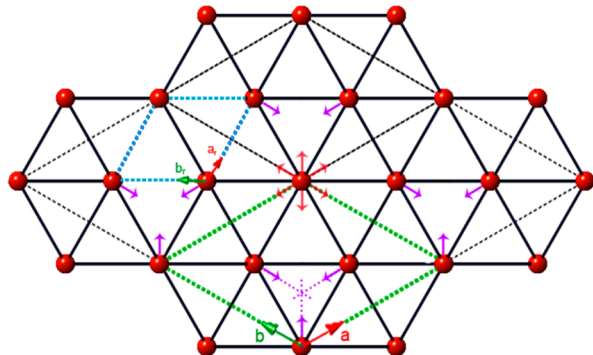


**Figure 1.** Schematic view of the V local displacements in the proposed trimers. Red balls denote the V positions in an undistorted structure ( $z = 0$ ), the blue dashed line represents the original rhombohedral lattice, and the green dashed line represents the superlattice. The purple arrows indicate the displacements of the  $\text{V}^{3+}$  ions starting with a  $\text{V}^{3+}$  ion at (0 0 0) in the undistorted lattice. The  $\text{V}^{3+}$  ions shift toward the center of a triangle (thick black line) forming a cluster. The red arrows show the directions of the other five possible displacements of a certain  $\text{V}^{3+}$  ion, suggesting 6 possible arrangements of V trimers in each layer.

complementary methods by which to study the local environments occurring in the present system. In particular, PDF analyses have recently proved to be an excellent tool for the study of the short-range ordering occurring in disordered Li ion battery electrodes.<sup>17–19</sup> While the X-ray PDF method is used here for the study of the local rearrangements involving V sites, it is less effective for Li-centered distortions because of the strong dependence of X-ray scattering length on atomic number. Insight into Li environments nevertheless remains a key target of the present study, given that the Li ions are directly involved in the electrochemistry of the material, and is provided here directly by MAS NMR Spectroscopy. The  ${}^6\text{Li}$  and  ${}^7\text{Li}$  isotopes are both NMR-active,  ${}^7\text{Li}$  (nuclear spin quantum number  $I = 3/2$ ) having a much higher natural abundance (92.5%) than  ${}^6\text{Li}$  ( $I = 1$ ) (7.5%) and a larger quadrupolar moment (albeit still very small compared with many other quadrupolar nuclei). However, the smaller gyromagnetic ratio of  ${}^6\text{Li}$  ( $\gamma_{\text{Li}}^7/\gamma_{\text{Li}}^6 = 2.6$ ) leads in paramagnetic phases to MAS spectra displaying reduced spinning sideband manifolds, and also usually provides higher resolution spectra because of the combination of a reduction in Li–Li homonuclear interactions with the lengthening of spin–lattice relaxation times. Various  ${}^6,7\text{Li}$  NMR studies of cathode materials show that such methods are well-suited to the characterization of Li insertion and deinsertion during cycling and to the study of defects and electronic structure.<sup>20–23</sup> Of particular relevance,  ${}^7\text{Li}$  and  ${}^{51}\text{V}$  NMR studies have already been performed on the stoichiometric materials  $\text{LiVS}_2$ <sup>24</sup> and  $\text{LiVO}_2$ ,<sup>25,26</sup> and are sensitive to the  $\text{V}^{3+}$ – $\text{V}^{3+}$ – $\text{V}^{3+}$  trimerization. The two signals observed in the  ${}^7\text{Li}$  NMR spectra of  $\text{LiVO}_2$  at 2.9 ppm ( $\beta_0$ ) and –1.1 ppm ( $\alpha_0$ ) were attributed by Takao et al. to the different Li environments within the layer caused by the formation of trimers.<sup>26</sup> Finally, while the presence of singlet state  $\text{V}^{3+}$ – $\text{V}^{3+}$ – $\text{V}^{3+}$  trimers in  $\text{LiVO}_2$  presents insurmountable difficulties for single-determinantal quantum mechanical calculations of the type pursued here, the electron–nuclear hyperfine interactions and magnetic exchange couplings occurring in  $\text{Li}_2\text{VO}_2$  may be extracted. The fact that relatively few details have been determined for this important end member phase provides an additional motivation for this study.

The main goal of the present study is to provide a detailed characterization of the Li and V environments occurring in the stoichiometric and lithium-excess materials, and to correlate such observations with the electrochemical performance. In the initial approach, PDF analyses are used to quantify the occurrence and distortions associated with  $\text{V}^{3+}$  trimerization in stoichiometric  $\text{LiVO}_2$ , and to investigate the range of excess Li contents over which the spin–lattice distortion persists. Li environments are then studied via solid state NMR to explore local changes on increase of excess Li content. In addition to the simpler one-pulse and echo experiments, structural information is derived from the recording of 2D POST-C7 (permutationally offset stabilized C7) spectra to probe Li–Li dipolar couplings,<sup>27,28</sup> and thereby determine the Li sites that are spatially close to each other. Finally, first principles DFT calculations of the  $\text{Li}_2\text{VO}_2$  phase are pursued, yielding useful data related to  $\text{V}^{2+}$ –O–Li pathway hyperfine contributions and magnetic exchange coupling constants.

## 2. EXPERIMENTAL AND THEORETICAL METHODS

**(a). Synthesis.**  $\text{Li}_{1+x}\text{V}_{1-x}\text{O}_2$  was synthesized by the reaction of  $\text{Li}_2\text{CO}_3$  and  $\text{V}_2\text{O}_3$  in the molar ratio  $1+x:1-x$ . Dried  $\text{Li}_2\text{CO}_3$  (Aldrich, 99%) and  $\text{V}_2\text{O}_3$  (Aldrich, 99%) powders were mixed together in a MBraun argon-filled drybox with a combined  $\text{O}_2$  and  $\text{H}_2\text{O}$  content of less than 1 ppm.  ${}^6\text{Li}_{1+x}\text{V}_{1-x}\text{O}_2$  samples were prepared in the same way using  ${}^6\text{Li}_2\text{CO}_3$  (Cambridge Isotope Laboratories, 95%). The mixture was placed in a gastight container (sealed with a cork gasket) and ball milled for 90 min (SPEX Centri-Prep 8000 M mixer/mill). The container was returned to the drybox and the powder transferred into an alumina crucible, which was covered with a lid. The mixture was then heated at 800 °C for 10 h under flowing argon (BOC). Once cooled to room temperature the compound was ground by hand in air and heated at 850 °C for 12 h under flowing 5% hydrogen in argon (BOC)<sup>7</sup>.

The phase purity of the  $\text{Li}_{1+x}\text{V}_{1-x}\text{O}_2$  samples was assessed by using X-ray powder diffraction, all samples being deemed to be phase pure on the basis of laboratory-based diffraction.<sup>7</sup>

**(b). Electrochemistry.** Composite electrodes were prepared by grinding together the active material in combination with Super S carbon and Kynar Flex 2801 binder in the mass ratio 80:10:10, respectively. Electrochemical cells containing the composite electrode, a lithium metal counter electrode ( ${}^6\text{Li}$  metal for the  ${}^6\text{Li}_{1+x}\text{V}_{1-x}\text{O}_2$  samples,  ${}^7\text{Li}$  metal for  ${}^7\text{Li}_{1+x}\text{V}_{1-x}\text{O}_2$ ), and the electrolyte [1 molar solution of  $\text{LiPF}_6$  in ethylene carbonate–dimethyl carbonate 1:1 ((v/v) Merck)] were assembled in the drybox. Cells were discharged to various depths at a rate of 10 mA g<sup>−1</sup> (at 30 °C) using a Maccor Series 4200 battery cycler. After discharge the cells were moved to the drybox where they were opened and the active material was recovered. The electrodes were rinsed with a small amount of dry solvent before being dried under dynamic vacuum for 2 h. Finally, the samples were stored in a glovebox.

**(c). PDF Analyses.** PDF analyses were performed on synchrotron X-ray total scattering data for pristine  $\text{LiVO}_2$  together with samples incorporating 3, 5, 7, and 10% of excess lithium ( $\text{Li}_{1.03}\text{V}_{0.97}\text{O}_2$ ,  $\text{Li}_{1.05}\text{V}_{0.95}\text{O}_2$ ,  $\text{Li}_{1.07}\text{V}_{0.93}\text{O}_2$ , and  $\text{Li}_{1.10}\text{V}_{0.90}\text{O}_2$ , respectively). Total scattering data were collected at room temperature using an amorphous Si 2D detector with an X-ray energy of 58 keV (wavelength  $\lambda = 0.21270 \text{ \AA}$ ) at beamline 11-ID-B at the Advanced Photon Source (APS) at Argonne National Laboratory.<sup>19</sup> The X-ray diffraction experiments were conducted in transmission geometry on finely powdered samples that were sealed in Kapton capillaries filled with argon gas. A  $\text{CeO}_2$  standard was used to calibrate the sample-to-detector distance and the tilt of the image plate relative to the beam path. Scattering measurements for the empty Kapton capillary were also performed under the same experimental conditions to obtain the instrumental background.<sup>29</sup> Intensity data versus  $2\theta$  and  $Q$  were obtained by converting the integrated image plate data using the Fit2D

software.<sup>30</sup> The PDF data were generated using the PDFgetX2 program.<sup>31</sup> Data corrections, including background subtraction, sample self-absorption, multiple scattering, X-ray polarization, Compton scattering, and Laue diffuse scattering were included to obtain the normalized total scattering structure function  $S(Q)$ .<sup>32</sup> The PDF  $G(r)$  was generated by direct Fourier transformation of  $Q[S(Q) - 1]$ , where the scattering wave factor  $Q = 4\pi \sin \theta/\lambda$ . A  $Q_{\max}$  of  $24.0 \text{ \AA}^{-1}$  was used, representing a trade-off between the size of the image plate and the sample-to-detector distance. Structure refinement and the fitting of  $G(r)$  were performed using the PDFgui software.<sup>33</sup> Previously collected scattering data for the Ni standard were processed and refined to obtain the instrumental damping factor. X-ray diffraction analysis was performed with the FullProf software.<sup>34</sup>

**(d). NMR Spectroscopy.**  $^{7}\text{Li}$  NMR studies were performed using rotor synchronized Hahn echo experiments with an evolution and refocusing period of one rotor cycle and a 1.8 mm probe designed by A. Samoson (spinning frequency = 35 kHz) on a 4.7 T Chemagnetics magnet. The  $\pi/2$  pulse length was  $1.38 \mu\text{s}$ .  $^{6}\text{Li}$  NMR spectra were recorded on a 9.4 T Bruker magnet using an Avance II console and a 4 mm probe. Rotor synchronized Hahn echo experiments (spinning frequency = 14 kHz) were used with one rotor cycle of evolution/refocusing. The  $\pi/2$  pulse length was  $4.50 \mu\text{s}$ . A POST-C7 sequence<sup>27,28</sup> was implemented using a spinning speed of 8 kHz, with 16 scans in the direct dimension. Double quantum evolution times of 2.50 and 1.75 ms were used for  $\text{LiVO}_2$  and  $\text{Li}_{1.07}\text{V}_{0.93}\text{O}_2$ , respectively. Hahn echo experiments were recorded using a recycle delay of 10 s while the 2D experiments used 100 s and 5 s for  $\text{LiVO}_2$  and  $\text{Li}_{1.07}\text{V}_{0.93}\text{O}_2$ , respectively, and were referenced to  $\text{LiCl}$  1 M at 0 ppm.

**(e). DFT Calculations.** First principles DFT calculations were performed within the CRYSTAL09 linear combinations of atomic orbitals code.<sup>35</sup> Two hybrid functionals were used, namely, the B3LYP functional [bearing 20% Hartree–Fock (HF) exchange] with a previously demonstrated satisfactory performance for the electronic structure and band gaps of a broad range of materials<sup>36</sup> and for the properties of transition metal compounds in particular,<sup>37</sup> and a related 35% HF functional previously shown to provide magnetic coupling constants in good agreement with experimental values.<sup>38–40</sup> In addition, recent calculations suggest that hybrid functionals with HF exchange in the range from 20 to 35% provide electron–nuclear hyperfine parameters in good agreement with experimental data.<sup>41</sup> Full details of the DFT calculations, including the basis sets and numerical parameters used, are presented in the Supporting Information, along with a detailed description of the electronic structure of the  $\text{Li}_2\text{VO}_2$  phase.

### 3. RESULTS

**(a). Bragg Diffraction.** The Bragg diffraction patterns (strictly, the total scattering data) of the  $\text{Li}_{1+x}\text{V}_{1-x}\text{O}_2$  samples, collected with synchrotron X-ray diffraction and subsequently converted to the  $2\theta$  values corresponding to  $\text{Cu K}\alpha_1$  radiation are shown in Figure 2. The experimental data are compared with the calculated diffraction pattern of the undistorted  $\text{LiVO}_2$  phase (i.e., the  $R\bar{3}m$  symmetry  $\alpha\text{-NaFeO}_2$  structure<sup>7</sup>). The experimental data are in excellent agreement with this simulated pattern, indicating that the undistorted model provides a good model for the long-range structure. However, a weak reflection at around  $2\theta = 21^\circ$  is seen in the patterns of all the samples, and a broad feature between  $2\theta = 18^\circ$ – $30^\circ$  emerges for  $\text{Li}_{1.10}\text{V}_{0.90}\text{O}_2$ , along with two new weak peaks at around  $2\theta = 28^\circ$  and  $32^\circ$ . The patterns are compared with the XRD pattern simulated for the distorted  $\text{LiVO}_2$  superstructure containing V trimers using the structural parameters discussed below; new reflections are certainly predicted to occur within this range. In particular, the weak reflection at  $2\theta = 21^\circ$  appears to be due to a combination of the two reflections appearing in the simulation at  $2\theta = 20.8^\circ$  and  $21.7^\circ$  and is therefore tentatively assigned to the superlattice reflections of  $\text{LiVO}_2$ , as

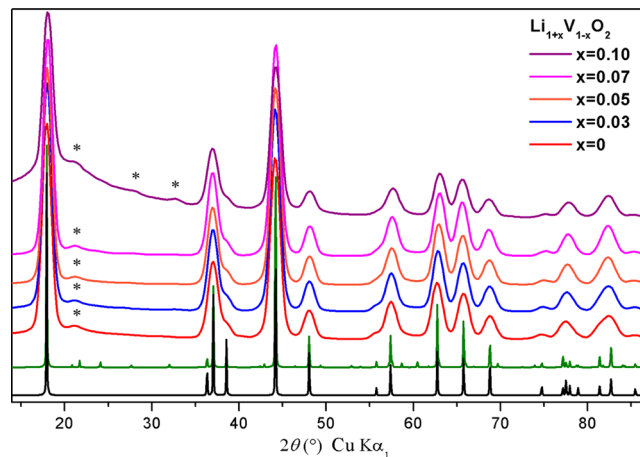


**Figure 2.** Experimental synchrotron XRD patterns for the  $\text{Li}_{1+x}\text{V}_{1-x}\text{O}_2$  series. The possible superlattice reflections are marked with asterisks. Two simulated patterns for  $\text{LiVO}_2$  are shown below, where the black pattern is simulated from the rhombohedral ( $R\bar{3}m$ ) structure and cell parameters reported by Armstrong et al.<sup>7</sup> and the green pattern is simulated from the refined superlattice structure (extracted from PDF data and described in the text). This structure is constructed based on the superlattice model proposed by Takao et al.<sup>26</sup>

previously discussed by Onoda and Tian<sup>15,16</sup> (see Figures S1–S3, in the Supporting Information). However, most of the superstructure peaks, if present, are apparently too weak to be detected by X-ray diffraction (XRD), most likely due to the short coherence length of the superstructure.

**(b). PDF Analysis of  $\text{Li}_{1+x}\text{V}_{1-x}\text{O}_2$ .** PDF analysis of the synchrotron diffraction data is plotted in the ranges from 0 to  $18 \text{ \AA}$  and from 18 to  $60 \text{ \AA}$  in Figures 3 and Supporting Information, Figure S4, respectively, similar plots being observed for all samples. The PDF pattern simulated using the undistorted  $\text{LiVO}_2$  structure ( $R\bar{3}m$  symmetry with cell parameters  $a = 2.8377 \text{ \AA}$ ,  $c = 14.8230 \text{ \AA}^7$ ) is very similar to the experimental profiles, if attention is restricted to intermediate-to-long-range (i.e., greater than approximately  $6 \text{ \AA}$ ). However, some noticeable discrepancies are observed between the experimental and the simulated profiles in the short (from approximately 2 to  $6 \text{ \AA}$ ) range. In particular, the peak in the simulated profile at  $2.8 \text{ \AA}$  corresponding to the first-shell V–V interatomic distance (marked B in Figure 3) does not occur in all of the experimental patterns, and is replaced by two new peaks at  $2.5$  and  $3.0 \text{ \AA}$  (marked D and E respectively in Figure 3), consistent with the presence of V trimers.<sup>26</sup> In the absence of trimerization, the six coplanar V–V interatomic separations per V site would be of equal length, whereas the presence of trimers leads to a displacement of each V cation to form two shorter and four longer coplanar V–V separations<sup>26</sup> with a predicted intensity ratio of 1:2, all of the latter being in good agreement with experimental findings. Furthermore, rather than a peak at approximately  $3.5 \text{ \AA}$  corresponding to V–O separations in the second coordination shell of the undistorted V cations (marked C in Figure 3), multiple peaks instead emerge in the experimental profiles (in the region marked F) attributable to the distortions of the  $\text{VO}_6$  octahedra because of the trimerization. The displacement of V atoms apparently does not vary significantly with increasing Li content, but there is a reduction in the intensities of the correlations, attributable in part to the decrease in V content.

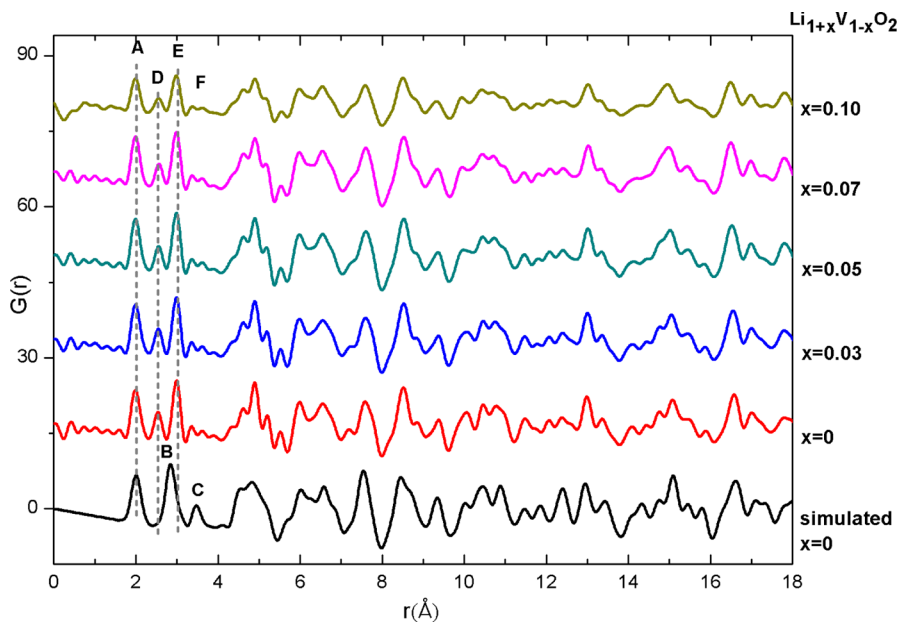


**Figure 3.** PDF analyses of  $\text{Li}_{1+x}\text{V}_{1-x}\text{O}_2$  plotted in the  $r$ -range from 0 to 18 Å. The pair correlations labeled A and C and the weaker features F correspond to V–O interatomic correlations while B, D, and E correspond to V–V interatomic correlations. The experimental PDF correlations are compared to those calculated with the  $\text{LiVO}_2$  rhombohedral structural model reported by Armstrong et al.<sup>7</sup>

**(c).  $^{6,7}\text{Li}$  NMR Studies of  $\text{Li}_{1+x}\text{V}_{1-x}\text{O}_2$ .**  $^7\text{Li}$  NMR. The local structure occurring in  $\text{Li}_{1+x}\text{V}_{1-x}\text{O}_2$  was initially investigated by  $^7\text{Li}$  NMR spectroscopy (Figure 4). First, resonances at

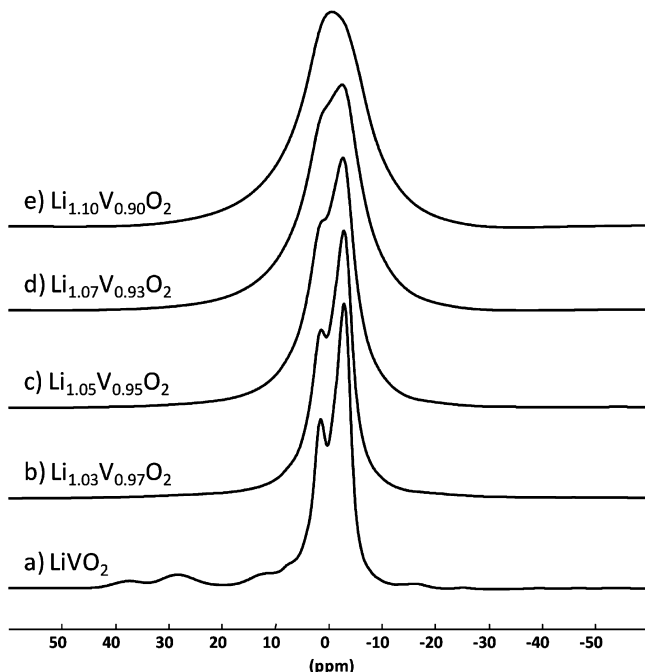


**Figure 4.**  $^7\text{Li}$  NMR spectra of  $\text{Li}_{1+x}\text{V}_{1-x}\text{O}_2$  with  $0 \leq x \leq 0.10$  recorded at 4.7 T with a spinning speed of 35 kHz.

approximately 0 ppm are observed in all spectra, in agreement with the previously published  $^7\text{Li}$  NMR of  $\text{LiVO}_2$ <sup>26</sup> and consistent with Li local environments that are not in the vicinity of paramagnetic species, in keeping with the suggested formation of a spin singlet trimerized state. Although the spectrum of the stoichiometric  $\text{LiVO}_2$  material (Figure 4a) is dominated by two signals at -2.9 and 1.1 ppm, other weak

resonances can be distinguished with shifts of 8, 12, 29, 37, -16, -24, -39, -47, and -54 ppm. These signals have previously been attributed to Li close to the  $\text{d}^1 \text{V}^{4+}$  ion,<sup>26</sup> and are an indication of the occurrence of Li-loss and  $\text{Li}_{1-x}\text{VO}_2$  formation in the nominally stoichiometric material. Consistent with this suggestion, the additional resonances disappear in the “Li-excess” materials, and the -2.9 ppm signal grows in intensity. The “0 ppm” signals also become broader and less well resolved, presumably because of an increase in the disorder of the material. Ionic and electronic mobility may also contribute to this broadening. When the inserted Li content reaches 7% ( $\text{Li}_{1.07}\text{V}_{0.93}\text{O}_2$ ), the -2.9 and 1.1 ppm resonances can no longer be separately resolved, a broad signal with a shoulder instead being observed. Meanwhile, only one broad signal is observed in the  $\text{Li}_{1.10}\text{V}_{0.90}\text{O}_2$  spectrum.

$^6\text{Li}$  NMR. Much sharper signals are seen in the  $^6\text{Li}$  NMR spectra of  $^6\text{Li}_{1+x}\text{V}_{1-x}\text{O}_2$  (Figure 5), presumably because of the reduction in the strengths of paramagnetic, quadrupolar and dipolar interactions relative to those observed in the  $^7\text{Li}$  NMR. Three resonances at 1.7, -1.4, and -2.9 ppm are now resolved in the spectra of  $\text{LiVO}_2$  and  $\text{Li}_{1.03}\text{V}_{0.97}\text{O}_2$ , the relative intensity of the resonance at -2.9 ppm growing slightly with increasing Li content (see Table 1). It is no longer possible to clearly distinguish the three resonances for excess Li contents greater than approximately 5% ( $\text{Li}_{1.05}\text{V}_{0.95}\text{O}_2$ ), suggestive of a more disordered structure and consistent with the observations from  $^7\text{Li}$  NMR. However, a shoulder at lower frequency is still resolved, along with a broader component spanning a width of more than 20 ppm.

The signals attributed to the presence of  $\text{V}^{4+}$  and Li deficiency in the Li layers in the  $^7\text{Li}$  NMR spectra are no longer present, which may indicate a lower degree of nonstoichiometry in the  $^6\text{Li}$ -enriched samples. However, the most likely explanation for the differences between the  $^6\text{Li}$  and  $^7\text{Li}$  samples is that the latter natural abundance samples, prepared earlier in the study, likely experienced a greater degree of air and/or moisture exposure, most probably during the NMR experi-

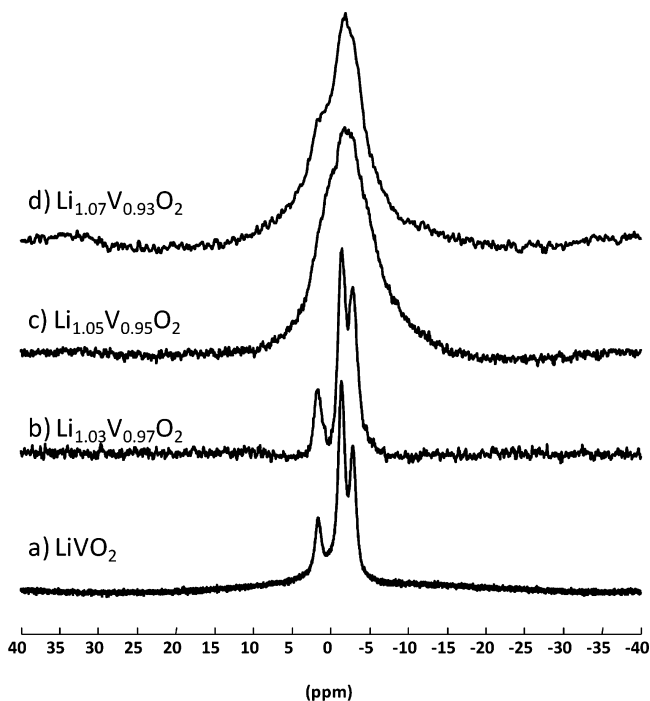


Figure 5.  ${}^6\text{Li}$  NMR spectra of  $\text{Li}_{1+x}\text{V}_{1-x}\text{O}_2$  with  $0 \leq x \leq 0.07$  recorded at 9.4 T with a spinning speed of 14 kHz.

**Table 1. Relative Intensities of the Three Peaks in the  ${}^6\text{Li}$  NMR Spectra for  $\text{LiVO}_2$  and  $\text{Li}_{1.03}\text{V}_{0.97}\text{VO}_2$**

material	resonance		
	1.7 ppm	-1.4 ppm	-2.9 ppm
$\text{LiVO}_2$	19.2	51.5	29.3
$\text{Li}_{1.03}\text{V}_{0.97}\text{O}_2$	16.3	46.3	37.4

ments. The effects appear to be more noticeable for materials with lower Li contents. Importantly, the two sets of samples illustrate the difference in the NMR spectra of Li excess and Li deficient materials, both sets of samples nominally containing

$\text{V}^{4+}$  ions the charges of which are compensated via different mechanisms.

Double quantum (DQ) filtered 2D experiments have been recorded for the stoichiometric  $\text{LiVO}_2$  and  $\text{Li}_{1.07}\text{V}_{0.93}\text{O}_2$  materials (Figure 6) to aid in the assignment of the  ${}^6\text{Li}$  NMR. The experiment should provide correlations between Li nuclei linked by  ${}^6\text{Li}$  homonuclear dipolar couplings, thereby identifying those pairs of nuclei that are both close in space and held rigidly in the lattice over the characteristic time scale of the experiment (approximately 10 ms). In general in 2D experiments, correlations between two signals with frequencies  $\nu_A$  and  $\nu_B$  will manifest as cross peaks at a position  $\nu_A + \nu_B$  in the DQ dimension, the individual signals appearing at  $\nu_A$  and  $\nu_B$  in the single quantum dimension. Off-diagonal cross peaks are clearly present in  $\text{LiVO}_2$  between the two signals at 1.7 and -2.9 ppm, suggesting that the two sites producing these resonances are in close proximity, likely in the same Li layer (Figure 6a). The separations between Li ions in the same and neighboring layers are 2.83 and 5.20 Å, respectively. In contrast, the only correlations involving the resonance at -1.4 ppm appear on the diagonal, indicating that these sites are close only to other ions of the same type. Weaker diagonal peaks are also seen for the 1.7 and -2.9 resonances, and a new, weak peak emerges at 0 ppm. In contrast, only very weak cross peaks are seen in the 2D spectrum of  $\text{Li}_{1.07}\text{V}_{0.93}\text{O}_2$  (Figure 6b). The spectrum is dominated by peaks along the diagonal, the main peak corresponding to the correlation involving the -1.4 ppm signal. There is a slight distortion in the spectrum that acts to rotate the positions of the cross peaks, the origin of which remains undetermined.

**Electrochemical Insertion of Li into  $\text{Li}_{1.07}\text{V}_{0.93}\text{O}_2$ .** The local structural changes occurring during the first discharge of a cell containing  $\text{Li}_{1.07}\text{V}_{0.93}\text{O}_2$  have been investigated by  ${}^6\text{Li}$  NMR (Figure 7). The electrochemistry is similar to that reported in the literature<sup>7</sup> and is shown in Figure S5 in the Supporting Information. The signal-to-noise ratio is poor because these spectra were recorded on  ${}^6\text{Li}$  natural abundance compounds. The  $0 \text{ mA h g}^{-1}$  sample corresponds to the pristine material, and gives rise to NMR spectrum consistent with the  ${}^7\text{Li}$  (Figure 4d) and  ${}^6\text{Li}$  (Figure 5d) spectra of  $\text{Li}_{1.07}\text{V}_{0.93}\text{O}_2$  discussed earlier. No noticeable changes are observed for the 10 and 20

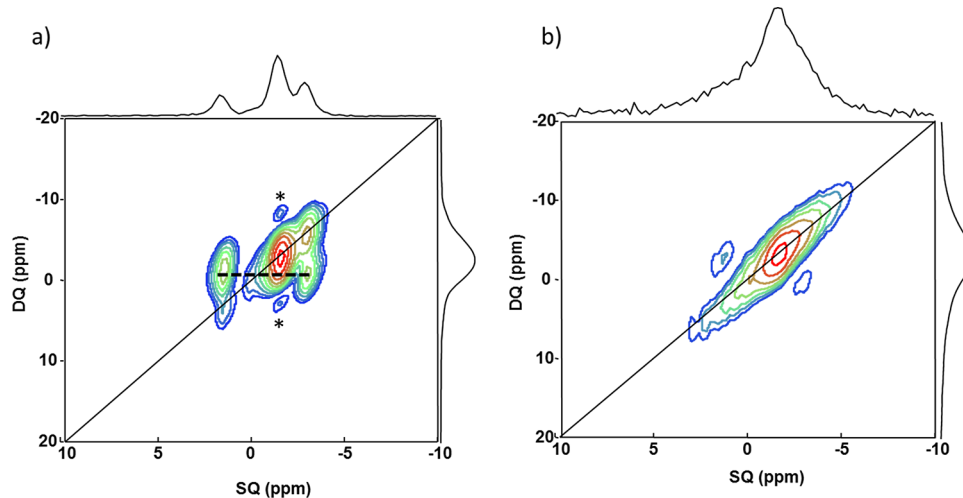
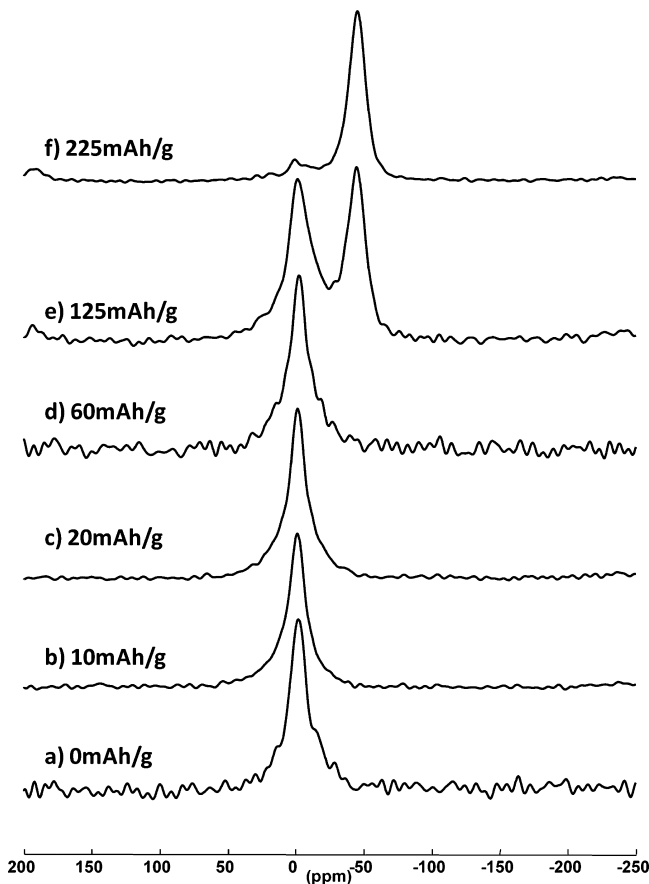


Figure 6. 2D postC7 spectra recorded at 9.4 T with a spinning speed of 8 kHz of (a)  $\text{LiVO}_2$  and (b)  $\text{Li}_{1.07}\text{V}_{0.93}\text{O}_2$ . The dashed line shows the cross peak between two peaks. The solid line is the diagonal connecting peaks in the single quantum (SQ) and double quantum (DQ) dimensions. The '\*'s in (a) represent artifacts due to truncation in the indirect dimension.



**Figure 7.**  ${}^6\text{Li}$  NMR spectra of materials extracted from batteries stopped during the first discharge; data were recorded at 9.4 T and 14 kHz.

$\text{mA h g}^{-1}$  samples, consistent with the prior assignment of the electrochemistry observed in the potential window from 2.5 to 0.1 V to solid electrolyte interphase (SEI) formation and electrolyte decomposition. Although previous work<sup>7</sup> identified the formation of an intermediate phase after  $60 \text{ mA h g}^{-1}$  of

discharge, no new signal was observed here by NMR. The lack of additional signal in this spectrum may possibly be associated with the poor signal-to-noise ratio. In light of this issue, further  ${}^7\text{Li}$  NMR experiments were performed (Supporting Information, Figure S6) but, as before, no additional signals were observed. It is possible that resonances may be rendered unobservable by virtue of being buried under the large manifold of  ${}^7\text{Li}$  sidebands, and future experiments will focus on NMR spectra acquired from  ${}^6\text{Li}$ -enriched materials. At  $125 \text{ mA h g}^{-1}$ , in addition to the 0 ppm signal, a second resonance is clearly resolved at approximately  $-45 \text{ ppm}$ . The  $-45 \text{ ppm}$  signal dominates the spectrum at  $225 \text{ mA h g}^{-1}$ , and can be assigned to the  $\text{Li}_{2+x}\text{V}_{1-x}\text{O}_2$  phase. The evolution of the signals with Li content is consistent with the presence of a two-phase reaction from  $\text{Li}_{1+y}\text{VO}_2$  to  $\text{Li}_2\text{VO}_2$ .  $\text{Li}_2\text{VO}_2$  contains  $\text{V}^{2+}$  d<sup>3</sup> ions which are thus isoelectronic with  $\text{Mn}^{4+}$  and  $\text{Cr}^{3+}$ . Our previous NMR studies of lithiated samples containing these ions have clearly shown that both negative and positive shifts can result, depending on the  $\text{Li}-\text{O}-\text{M}$  bond angles.<sup>23</sup> The tetrahedrally coordinated Li site in  $\text{Li}_2\text{VO}_2$  has three  $\text{Li}-\text{O}-\text{V}$  angles of  $125^\circ$ , three at  $165^\circ$ , and six at  $79^\circ$ , the overall negative shift indicating the dominance of a polarization contribution (presumably resulting from the three  $165^\circ$   $\text{Li}-\text{O}-\text{V}$  angles), a mechanism which does not involve direct overlap of a d electron containing an unpaired electron.<sup>7</sup> The predominance of this mechanism over delocalization (in cases where bond angles allowing both mechanisms to occur are present) is consistent with findings for  $\text{Cr}^{3+}$  compounds such as  $\text{LiCrO}_2$  and  $\text{La}_4\text{LiCrO}_8$ .<sup>42</sup> We now explore the shift mechanism via the DFT calculations reported in the next section.

**(d). DFT Calculations for  $\text{Li}_2\text{VO}_2$ .** Given a general lack of data, DFT calculations have been performed for the  $\text{Li}_2\text{VO}_2$  end member phase, with a focus upon magnetic coupling constants and Li hyperfine parameters (a full analysis of the electronic structure being presented in the Supporting Information). The magnetic coupling constants were computed in part so as to allow connections to be made with the room temperature NMR hyperfine shifts. First, the geometry optimizations, performed within the ferromagnetic (FO) state

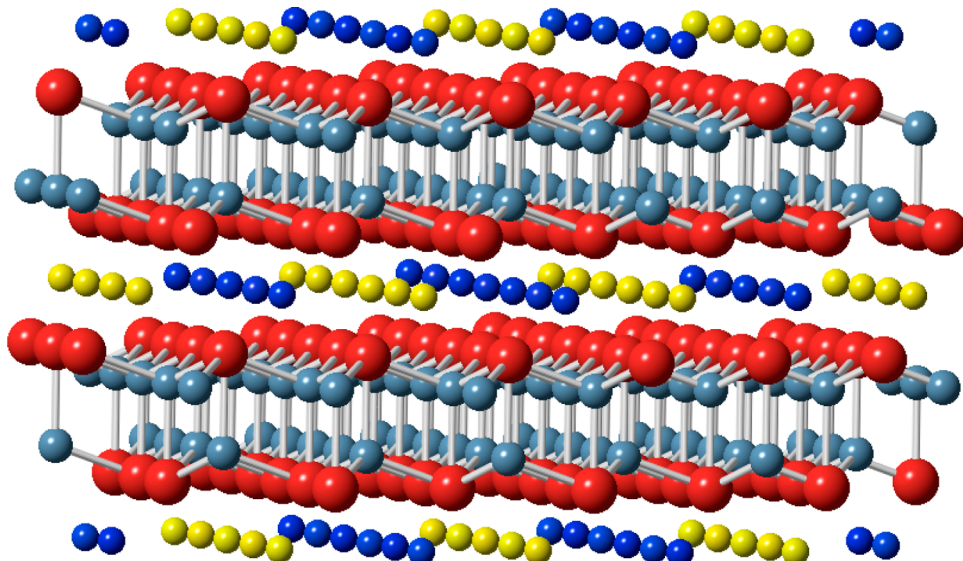


**Figure 8.** Optimized ground AF2 magnetic state of  $\text{Li}_2\text{VO}_2$ . Dark blue, yellow, red, and lighter blue atoms denote spin-up V, spin-down V, O, and Li sites, respectively.

**Table 2. Hyperfine shifts,  $\delta_{\text{iso}}$  (ppm), Pathway Contributions,  $P_1$  to  $P_3$  and  $P_d$  (As Defined in Text, ppm), and Sum of the Pathways  $\sum_i z_i P_i$  for  $\text{Li}_2\text{VO}_2$  as a Function of Hybrid Functional Applied, Structures, and Effective Weiss Temperature  $\Theta$**

hybrid	structure	$\Theta$	$\delta_{\text{iso}}$	$P_1^a$	$P_2^b$	$P_3^c$	$P_d^d$	$\sum_i z_i P_i$
20% HF	optimized FO	-605.5	-100.7	-22.9	+19.4	-29.3	0.0	-98.6
		-807.4	-82.7	-18.8	+15.9	-24.1	0.0	-80.9
	optimized AF2	-605.5	-107.1	-22.2, -27.2, -27.1	+22.8, +20.9, +20.9	-31.1	-0.2	-105.6
		-807.4	-88.0	-18.2, -22.3, -22.3	+18.7, +17.2, +17.2	-25.5	-0.1	-86.7
	experiment	-605.5	-111.1	-26.5	+23.0	-32.8	-0.2	-109.4
		-807.4	-91.2	-21.7	+18.9	-26.9	-0.2	-89.8
35% HF	optimized FO	-464.8	-184.2	-47.2	+19.5	-32.5	-0.3	-181.6
		-624.5	-153.0	-39.2	+16.2	-27.0	-0.2	-150.9
	optimized AF2	-464.8	-189.9	-46.3, -50.4, -50.3	+22.6, +20.9, +20.9	-34.2	-0.4	-186.4
		-624.5	-157.8	-38.5, -41.9, -41.8	+18.8, +17.3, +17.3	-28.4	-0.3	-154.9
	experiment	-464.8	-193.9	-49.7	+22.6	-36.2	-0.5	-191.6
		-624.5	-161.1	-41.1	+18.7	-30.1	-0.4	-159.2

<sup>a</sup>The  $P_1$  pathways are split by the spin–lattice distortion in the optimized AF2 structure into  $d = 2.598, 2.628$ , and  $2.628 \text{ \AA}$  with angles  $\alpha = (77.60, 77.61), (78.87, 79.12)$  and  $(78.87, 79.12)^\circ$ , respectively. <sup>b</sup>Similarly, the  $P_2$  pathways are split into  $d = 3.729, 3.738$ , and  $3.738 \text{ \AA}$  with angles  $\alpha = 124.72, 124.92$  and  $124.91^\circ$ , respectively. <sup>c</sup>The  $P_3$  pathways are split into  $d = 4.066, 4.092$ , and  $4.092 \text{ \AA}$  with angles  $\alpha = 164.47, 164.38$  and  $164.37^\circ$ , respectively, but split pathway contributions cannot be determined in the AF2 supercell. <sup>d</sup>The distant  $P_d$  contributions are split into  $d = 4.849, 4.889$ , and  $4.889 \text{ \AA}$ , but, again, split contributions cannot be determined in the AF2 supercell.

using the 20% HF hybrid and BS–I sets (see Supporting Information), reproduce the experimental structure<sup>7</sup> well, yielding a maximal deviation of 2.4% of experiment from the hexagonal  $a$  and  $c$  cell parameters and  $w_{\text{Li}}$  and  $w_{\text{O}}$  internal coordinates. Proceeding within the optimized structure, the total energies of the FO and five distinct antiferromagnetic (AF) states were obtained within a  $2 \times 2 \times 2$  supercell expansion of the hexagonal  $\text{Li}_2\text{VO}_2$  primitive cell.

Fitting of a magnetic Hamiltonian  $H = \sum_{ij} (J_{ij}/2) \mathbf{S}_i \cdot \mathbf{S}_j$  to the total energies yields average nearest–neighbor in-plane (IP) and out-of-plane (OOP) magnetic coupling constants  $J_{\text{IP}} = 80.7 \text{ K}$  (standard deviation  $\sigma = 0.2 \text{ K}$ ) and  $J_{\text{OOP}} = -0.1 \text{ K}$  ( $\sigma = 0.3 \text{ K}$ ) with the 20% HF hybrid, and  $J_{\text{IP}} = 61.9 \text{ K}$  ( $\sigma = 0.2 \text{ K}$ ) and  $J_{\text{OOP}} = -0.1 \text{ K}$  ( $\sigma = 0.3 \text{ K}$ ) at 35% HF, where positive  $J$  denotes an AF coupling. The large standard deviations obtained for the very small  $J_{\text{OOP}}$  coupling indicate that the precise size and even sign of this interaction cannot be regarded as reliable, but it is clearly much smaller in magnitude than the dominant IP coupling. The effective Weiss temperature may be computed in the mean field approximation as  $\Theta = -(1/3k_{\text{B}})(6|J_{\text{IP}}| + 2|J_{\text{OOP}}|)S(S+1)$ , where  $k_{\text{B}}$  is the Boltzmann constant and  $S = 3/2$  is the formal spin of the  $\text{V}^{2+}$  centers, yielding values of -605.5 and -464.8 K in the 20 and 35% HF hybrids, respectively, indicative of very strong remnant IP AF correlations in the paramagnetic state. The tendency to form a long-range ordered state at all but the lowest temperatures will be strongly suppressed by the very small magnitude of  $J_{\text{OOP}}$ , so that the magnetic state of the crystal may be envisaged as comprising strongly AF correlations within the (001)  $\text{V}^{2+}$  planes and essentially negligible correlations between the planes. Some degree of magnetic frustration must, of course, be present within the planes, where, in the lowest energy AF state obtained here (denoted AF2, see Figure 8), each V site has two and four IP nearest-neighbors sites bearing parallel and antiparallel moments, respectively, and two OOP nearest-neighbors with antiparallel moments, each (001)  $\text{V}^{2+}$  plane comprising FO [110] chains arranged in an alternating AF order. Subsequent geometry optimizations in the AF2 state reveal the presence of a significant spin–lattice effect, where, proceeding from optimized FO IP and OOP V–V distances of 3.176 and 5.097  $\text{\AA}$ , respectively, the four energetically favorable IP AF

exchange pathways decrease in length to 3.120  $\text{\AA}$ , the disfavored IP FO pathways, to 3.162  $\text{\AA}$ , and the weaker OOP pathways increase in length to 5.160  $\text{\AA}$ . Clearly, given the small magnitude of  $J_{\text{OOP}}$ , the latter effect is unlikely to be driven by a spin–lattice interaction, but is more probably a longer ranged structural accommodation of the relaxation of the V cations within the (001) planes. The additional stabilization of the optimized AF2 state induced by the distortion (derived as the difference in energies of the AF2 state in the optimized FO and AF2 structures) amounts to 1.3 kJ/mol in the 20% HF hybrid, while the maximal error in structural parameters relative to experiment falls to 1.2%, a finding that may indicate the presence of weak distortions of this type in the experimental structure. Coincidentally, in this system, the thermal equivalent of half the magnetic energy difference  $\Delta E_{\text{mag}} = E(\text{AF2}) - E(\text{FO})$  per V site amounts to  $-(1/k_{\text{B}})(2J_{\text{IP}} + J_{\text{OOP}})S(S+1)$ , which, ignoring the small difference in the OOP contribution, should lie very close to the  $\Theta$  parameter derived above. Computing  $\Delta E_{\text{mag}}/2k_{\text{B}}$  in both the optimized FO and AF2 geometries yields approximate  $\Theta$  values of -604.3 and -807.4 K, respectively, in the 20% HF hybrid; and -463.9 and -624.5 K, respectively, at 35% HF exchange, where the values derived in the FO structure are very close to the more formally correct  $\Theta$  temperatures presented above. It is clear from this that the partial alleviation of frustration in the AF2 optimized structure significantly strengthens the IP AF ordering, where the increase in  $\Delta E_{\text{mag}}$ , if attributed entirely to IP coupling, leads to an increase in average  $J_{\text{IP}}$  to values 107.7 and 83.3 K in the 20 and 35% HF hybrids, respectively, an enhancement of approximately 34 to 35% of the undistorted IP couplings.

Finally, the electron–nuclear Li hyperfine parameters have been computed using the more extensive BS–II sets (see Supporting Information) for the 20% and 35% HF hybrids in both optimized FO and fixed experimental<sup>7</sup> structures. The method is identical to that adopted in a recent study of a range of  $\text{Fe}^{3+}$  phosphates,<sup>41</sup> briefly, neglecting pseudocontact and zero field splitting effects, the Fermi contact contribution to the Li hyperfine shift is computed from the spin density directly at the Li nucleus obtained within the FO state, and finally scaled to a value consistent with the experimental paramagnetic state by multiplication by a factor  $\Theta = B_0 \mu_{\text{eff}}^2 / 3k_{\text{B}} g_{\text{e}} \mu_{\text{B}} S(T - \Theta)$ ,

where  $B_0$  is the static magnetic induction;  $\mu_{\text{eff}}$  the effective magnetic moment per V site;  $g_e$  the free electron  $g$ -value;  $\mu_B$ , the Bohr magneton; and  $T$  the temperature (assumed equal to 320 K throughout to account for the effects of frictional heating due to MAS). Here  $\mu_{\text{eff}}$  is assumed equal to the  $d^3$  spin-only value of 3.873  $\mu_B$  throughout. Correction for the effects of spin-orbit coupling in the  ${}^4\text{A}$  ground state term of octahedral  $\text{V}^{2+}$  was considered, but neglected on the grounds that it reduces the spin-only moment by only approximately 3% at most.<sup>43</sup>

The contributions of successive  $\text{V}^{2+}$  cation shells to the Li shift are also determined, via the flipping (i.e., spin-up to spin-down) out of fully FO order of selected  $\text{V}^{2+}$  moments in the  $2 \times 2 \times 2$  supercell. Three shells of Li–O–V pathways ( $P$ ) are found to be of consequence, with geometry in the FO optimized structure as follows: the double path  $P_1$  with Li···V distance  $d = 2.616 \text{ \AA}$  and Li–O–V angles  $\alpha = 2 \times 77.87^\circ$  (experimental  $d = 2.635 \text{ \AA}$  and  $\alpha = 2 \times 79.48^\circ$ ); the single path  $P_2$  with  $d = 3.715 \text{ \AA}$  and  $\alpha = 123.94^\circ$  (experimental  $d = 3.751 \text{ \AA}$  and  $\alpha = 125.11^\circ$ ); and the single path  $P_3$  with  $d = 4.114 \text{ \AA}$  and  $\alpha = 165.08^\circ$  (experimental  $d = 4.074 \text{ \AA}$  and  $\alpha = 165.31^\circ$ ). A fourth shell “distant” contribution, denoted  $P_d$  below, is also considered, although it is likely to be weak given that it does not correspond to a direct  $\text{V}^{2+}$ –O–Li pathway. The accuracy of the decomposition of the total shifts into pathway contributions can be tested by comparing the original calculated shift with the sum  $\sum z_i P_i$ , where the  $\text{V}^{2+}$  coordination number  $z_i = 3$  for all pathways. The splittings of the  $P_1$  and  $P_2$  pathway contributions due to the spin-lattice distortion in the optimized AF2 state are also determined; the analogous splittings in  $P_3$  and  $P_d$  contributions cannot be separately determined in the AF2 supercell, average values therefore being presented for the latter interactions.

Total shifts and pathway contributions are presented in Table 2. The calculations all reproduce the negative sign of the isotropic hyperfine shift in  $\text{Li}_2\text{VO}_2$ , assigned at  $-45 \text{ ppm}$  in the experimental spectroscopy above. However, the magnitude of the shift is overestimated by all functionals in each structure considered, the value obtained from the 20% HF hybrid in the optimized FO structure being closest to experiment at approximately  $-83 \text{ ppm}$ . The presence of a significant concentration of V cations in higher oxidation state in the real  $\text{Li}_{2+x}\text{V}_{1-x}\text{O}_2$  sample may be an important factor contributing to this discrepancy, as may the use of the mean field approximation in deriving effective  $\Theta$  values. However, the deviations observed here are broadly comparable to rms errors ranging up to  $91 \text{ ppm}$  obtained previously from similar Li shift calculations across a set of  $\text{Fe}^{3+}$ -containing materials.<sup>41</sup>

The decomposition of the directly calculated total Li shifts into  $P_1$ ,  $P_2$ ,  $P_3$ , and  $P_d$  pathway contributions is confirmed as accurate by comparison of the former with the sum of the latter, leading in all cases to differences amounting to less than 2.5% of the former values. The distant  $P_d$  contributions are confirmed as negligible in all cases considered. Examining the significant pathway decompositions in detail, the near  $80^\circ$   $P_1$  interactions provide negative contributions, an unexpected finding given that the idealized  $90^\circ$   $\text{V}(\text{t}_{2g}^{\alpha})$ –O( $p_{\pi}$ )–Li(s) orbital interaction would be expected to yield a positive shift due to a straightforward delocalization mechanism. The closing of the  $P_1$  angle in the optimized and experimental structures from the idealized  $90^\circ$  geometry must, of course, shorten the direct Li···V separation, potentially leading to a significant overlap of  $\text{V}(\text{t}_{2g}^{\alpha})$  and Li(s) orbitals and to polarization of the

latter. At the other extreme of angle, the approximately  $165^\circ$   $P_3$  interactions also yield negative shifts, in keeping with the understanding that pathways similar in geometry to the idealized  $180^\circ$   $\text{V}(\text{e}_g^0)$ –O( $p_{\sigma}$ )–Li(s) pathway should lead to negative contributions due to polarization by the occupied  $\text{V}(\text{t}_{2g}^{\alpha})$  orbitals. Finally, the near  $125^\circ$   $P_2$  pathways provide a positive contribution; rationalization of shifts on the basis of orbital overlap is difficult at intermediate angles, but it is clear that the  $\text{V}(\text{t}_{2g}^{\alpha})$ –O( $p_{\pi}$ )–Li(s) delocalization mechanism must dominate over other effects in this case. The pathway contributions derived in this way are expected to find use in rationalizing NMR spectra obtained from doped and/or partially delithiated materials.

## ■ DISCUSSION

**Structural Model for  $\text{Li}_{1+x}\text{V}_{1-x}\text{O}_2$ .** Both the NMR and X-ray analyses provide clear evidence for local structural distortions persisting throughout the whole  $\text{Li}_{1+x}\text{V}_{1-x}\text{O}_2$  series that are not representable within a simple structural model based on rhombohedral  $\text{LiVO}_2$ . Making use of both experimental NMR and PDF, we now construct a model capturing some of the important distortions. We start by considering a single V layer, constructing a 2D supercell from the undistorted 2D rhombohedral unit cell.<sup>7,26</sup> The new  $\mathbf{a}$  and  $\mathbf{b}$  lattice parameters (green dashed lines, Figure 1) are defined by  $\mathbf{a}_r - \mathbf{b}_r$  and  $\mathbf{a}_r + 2\mathbf{b}_r$  respectively, where  $\mathbf{a}_r$  and  $\mathbf{b}_r$  are the lattice parameters of the original rhombohedral cell (blue dashed lines, Figure 1). The  $P1$  space group is used hereafter for its flexibility in the representation of the V distortions in the subsequent analysis and for the reason that it simplifies the analysis in three dimensions. The displacement model was constructed by assuming that each  $\text{V}^{3+}$  ion shifts toward the center of a triangle formed by three  $\text{V}^{3+}$  ions, forming trimers within the (001) V planes, as shown in Figure 1. A magnitude  $0.17 \text{ \AA}$  of the displacement of each  $\text{V}^{3+}$  cation was extracted from a simple geometrical calculation on the basis of the first coordination shell V–V interatomic distances (atomic pairs D and E) observed in the PDF patterns (Figure 3), which correspond to the intra- (D) and shortest inter-trimer (E) V–V distances. Proceeding on the assumption that the local distortions of the  $\text{V}^{3+}$  ions are homogeneously distributed throughout each (001) V layer, specification of the direction of displacement of one  $\text{V}^{3+}$  ion suffices to determine the positions of all remaining  $\text{V}^{3+}$  ions within the same layer. Given that each  $\text{V}^{3+}$  has six possible displacement vector orientations (the six red arrows shown in Figure 1), six possible (symmetry related) arrangements of the trimer clusters emerge within each layer, relative to the positions of  $\text{V}^{3+}$  ions in a notionally undistorted 2D layer. The six possible arrangements become important only when we consider the 3D packing of V layers along the hexagonal  $c$ -axis, generating six distinct stacking arrangements in a two V-layer supercell and 36 in a three V-layer cell, all as derived from cubic close packing. The latter supercell size provides a significantly greater degree of structural freedom and is used hereafter, leading to 36 distinct unit cells. Clearly, some of these 36 cells are symmetry related, an issue discussed later along with the effect of the Li layer stacking. We note that there is no a priori requirement that the packing of the trimer layers should repeat over an interlayer separation consistent with three V layers; many stacking sequences are possible, alongside the possibility that the material displays complete structural disorder. However, to choose a tractable structural model for the further analysis of the scattering data, a series of preliminary

refinements of the 36 candidate cells were performed, fitting to the PDF data for the LiVO<sub>2</sub> sample over distances (*r*-range hereafter) ranging from 1.6 to 10 Å. Given that variations in the local coordination geometries of the V<sup>3+</sup> ions were most evident over short distances (see Figure 3), most of the short-range structural information is expected to be reliably captured by these models, albeit that the intermediate to long-range order may not be modeled correctly. The weighted agreement R-factors (Rw)<sup>29</sup> of the structural refinements of the 36 candidate cells varied from 19.96 to 24.25%, where 27 of the structural models yield an Rw less than or equal to 20.7%, and the remaining nine yield Rw values greater than 22.2% (see Supporting Information, Figure S7). The structure with the lowest Rw = 19.96% was adopted as the model superlattice unit cell (Figure 9), and its atomic positions are given in the

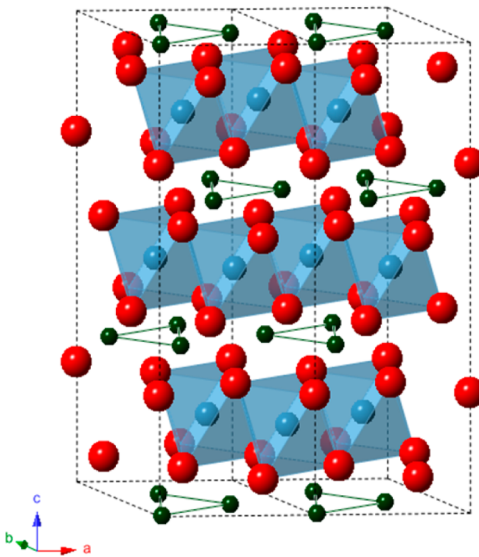


**Figure 9.** Supercell structure employed for PDF refinement, in which Li (blue), V (dark green), and O (red) ions occupy alternating (111) planes, ABC-stacking occurring along the *c*-axis direction.

Supporting Information, Table S1. The precise V arrangement and stacking sequence occurring in this cell will be discussed later. The simulated XRD pattern calculated for this superstructure is shown in Figure 2 (green pattern). As discussed earlier, the most noticeable additional reflections occur in the range from  $2\theta = 20^\circ$  to  $35^\circ$ , while the weak reflection observed experimentally at approximately  $21^\circ$  in all samples may reasonably be assigned to an overlap of the first two additional reflections (see the Supporting Information for a more detailed discussion and indexing of these reflections in the new superstructure cell). The two simulated reflections occurring at approximately  $2\theta = 28^\circ$  and  $32^\circ$  may account for the further two weak reflections that are clearly observed only in the Li<sub>1.10</sub>V<sub>0.90</sub>O<sub>2</sub> sample. We note that the broad background occurring in the experimental pattern obtained from the Li<sub>1.10</sub>V<sub>0.90</sub>O<sub>2</sub> sample does not appear to give rise to distinct correlations in the PDF patterns. The presence of such a background only for this sample may be indicative of increased disorder.

We use the supercell model derived above to perform a more detailed refinement of the short to long-range structure (from 1.6 to 60 Å) (Figure 10). Initially, both the Li and the O atomic positions were fixed, refining only the V atom positions. The V

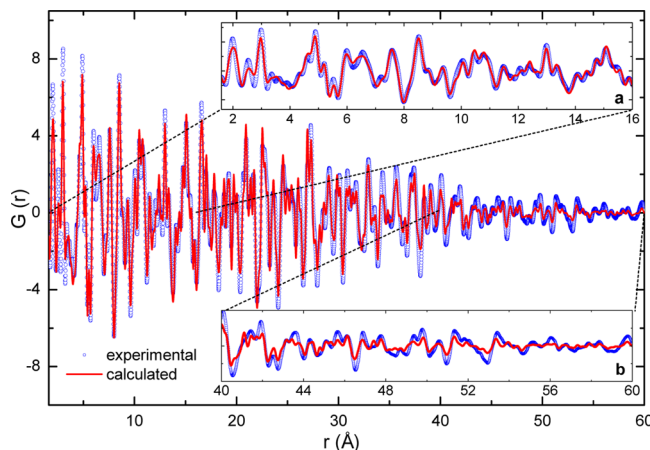


**Figure 10.** PDF refinement of LiVO<sub>2</sub> (with fixed O atomic position) in the *r*-range of 1.6–60 Å (Rw = 31.64%). Two insets are the zoomed-in regions of 1.6–16 Å and 40–60 Å, red = calculated pattern, blue = experimental pattern.

displacement parameters within each layer were constrained to be equal, but were allowed to vary between layers. The quality of the fit varied dramatically with *r*-range, resulting in an overall Rw = 31.64% for the full 1.6 to 60 Å range. Note that Rw is higher than above because a larger data range is used in the refinements. Good agreement between the experimental and calculated pattern is obtained at short-range (*r*-range 1.6 to 16 Å; top inset in Figure 10a), whereas significant deviations are noted at longer range (*r*-range 40 to 60 Å; bottom inset in Figure 10b). Taken together, these findings suggest that the local distortions present in the V<sup>3+</sup> layers are reasonably well accounted for, but that the long-range ordering is not accurately represented. Since the quality of the fit varies significantly with the *r*-range considered, individual refinements were performed in three distinct *r*-ranges, namely, 1.6 to 16 Å, 16 to 30 Å, and 30 to 60 Å, so as to obtain a better understanding of the V distortions. The first range was chosen to capture the inter- and intra layer correlations, while the third captures the longer *r*-range correlations. The refinement of the 1.6 to 16 Å data yielded an Rw = 22.00% and a slightly better fit to peaks D and E (Figure 11a) over that obtained in the refinement shown in Figure 10. In addition, the multiple peaks in region F at around 3.5 Å are now captured by the calculated pattern. However, the width of peak A is sharper in the experimental data, suggestive of a less distorted V local environment and a narrower distribution of V–O distances. The refinements of the 16 to 30 Å and 30 to 60 Å data yielded Rw = 22.20% (Figure 11b) and 25.65% (Figure 11c), respectively, which suggests that both the intermediate and the long-range structure of LiVO<sub>2</sub> can be reasonably well represented by the trimer superstructure. To explore the local distortions in more detail, further refinements of the model superstructure were performed over the shortest range from 1.6 to 16 Å by allowing completely free displacements of both V and O atoms. An excellent fit with a dramatic reduction in Rw to 10.19% (Figure 12) was obtained, suggesting that an improved description of the local displacements is achieved. The structural data is given in the Supporting Information, while the V–O and V–V distances are given in Table 3, average values of 2.54(2) and 3.00(2) emerging for the latter, corresponding to V–V separations within and between trimers, respectively. The corresponding displacement magnitudes of V atoms from their normal

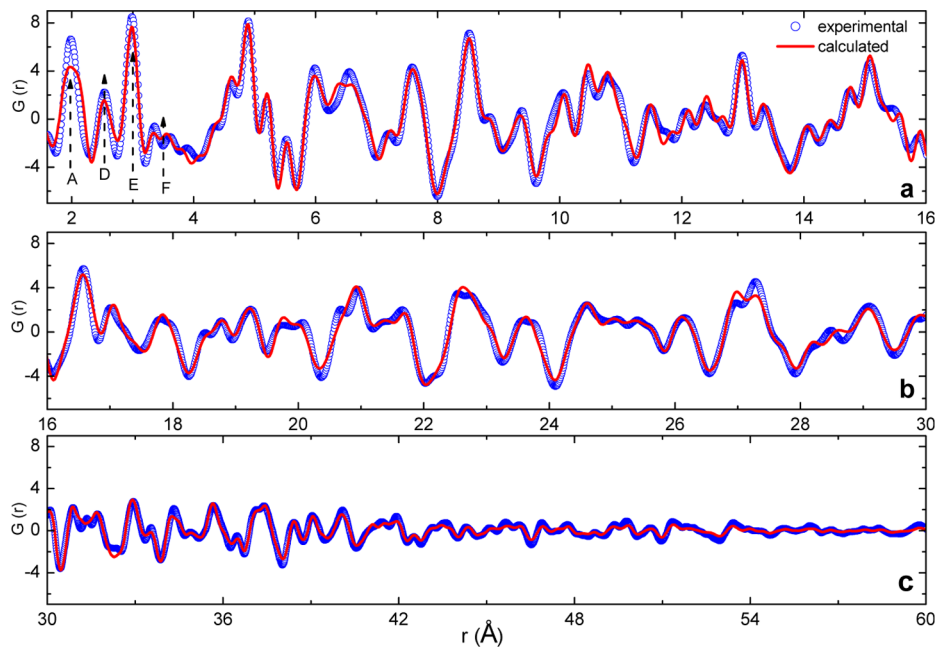


**Figure 11.** PDF refinement for  $\text{LiVO}_2$  (with fixed O atomic positions) in the short, intermediate and long-range. (a)  $1.6\text{--}16\text{ \AA}$  ( $\text{R}_\text{w} = 22.00\%$ ). (b)  $16\text{--}30\text{ \AA}$  ( $\text{R}_\text{w} = 22.20\%$ ). (c)  $30\text{--}60\text{ \AA}$  ( $\text{R}_\text{w} = 25.60\%$ ). Peak A and the wiggles, F, correspond to V–O interatomic correlations, D and E correspond to V–V interatomic correlations, red = calculated pattern, blue = experimental pattern.

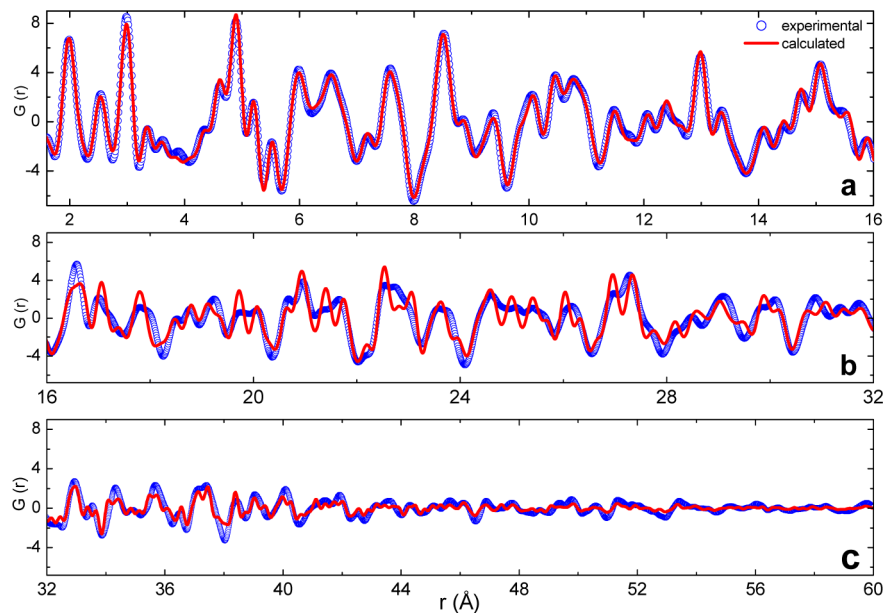


**Figure 12.** (a) PDF refinement for  $\text{LiVO}_2$  (where the O atomic position is now refined) in the range from  $1.6\text{--}16\text{ \AA}$  ( $\text{R}_\text{w} = 10.19\%$ ). (b) The  $1.6\text{--}32\text{ \AA}$  and (c)  $32\text{--}60\text{ \AA}$  range of the simulated pattern for  $\text{LiVO}_2$ , using the structure refinement shown in (a) ( $\text{R}_\text{w} = 35.13\%$ ), red = calculated pattern, blue = experimental pattern.

positions in the ideal  $\alpha\text{-NaFeO}_2$  structure amounts to  $0.17(2)$   $\text{\AA}$ . In contrast, a simulation of the PDF pattern in the whole  $r$ -range from  $1.6$  to  $60\text{ \AA}$ , on the basis of the superstructure refined solely from the short-range data (as just described), yields a poor fit at intermediate and longer distances with an  $\text{R}_\text{w} = 35.13\%$  (Figures 12b and 12c). The fit is worst at intermediate ranges (Figure 12b), which may be due to variations and increased disorder in the stacking order of the V trimers that are not captured in the structural model. Such effects will be less apparent at longer distances.

We now use the derived structural model to analyze the NMR data in more detail. The  $\text{V}^{3+}$  ion in  $\text{LiVO}_2$  has a  $d^2$  electronic configuration and thus, in principle, has two unpaired electrons. The  $^{67}\text{Li}$  NMR spectra of paramagnetic materials typically show broad lineshapes, large hyperfine shifts, and short nuclear relaxation times.<sup>23,44</sup> However, as discussed above, the occurrence in  $\text{LiVO}_2$  of antiferromagnetic exchange, and orbital ordering and polarization leads to the formation of singlet state  $\text{V}^{3+}$  trimers,<sup>10</sup> thereby explaining the small chemical shifts around  $0$  ppm observed in the  $^{67}\text{Li}$  NMR spectra, along with the long relaxation time (of a few seconds) and relatively sharp

**Table 3. Average V–O and V–V Atomic Pair Correlations and Standard Deviations (Å) Obtained from the Structure Reported in Supporting Information, Table S2**

atomic pairs	distance	standard deviation
V–O	1.81	0.10
V–O	1.93	0.05
V–O	1.98	0.04
V–O	2.03	0.02
V–O	2.11	0.07
V–O	2.23	0.13
V–V	2.53	0.01
V–V	2.55	0.03
V–V	2.98	0.00
V–V	2.99	0.01
V–V	3.00	0.01
V–V	3.01	0.01

signals. An explanation for the multiple resonances emerges from a consideration of the effects of  $\text{V}^{3+}$  trimerization on the Li local environments. On the basis of the 2D NMR spectrum of the stoichiometric material, three major local environments can be resolved, where the two giving rise to the 1.7 and –2.9 ppm signals most likely reside in the same layer. The third Li site corresponding to the signal at –1.4 ppm lies further away in the structure from the other two. At least two hypotheses may be proposed: first, that the third Li occupies an octahedral site of the nominally  $\text{V}^{3+}$  layer, filling a V vacancy; or second, that three Li environments occur in the alkali metal layer rather than the two identified previously.<sup>26</sup> The first hypothesis appears unlikely, since the –1.4 ppm resonance corresponds to a significant fraction of the Li content (see Table 1). To explore the second hypothesis, the possible Li environments resulting from trimerization are now considered (Figure 13). Considering first a single  $\text{V}^{2+}$  layer, Li may be stacked in the layer(s) above and below so as to yield two different sets of local environments. In Figure 13a, one Li lies directly above a trimer (i.e., above the face of the trimer), while two do not (and are, instead, corner-shared with three trimers); these environments are labeled as Li(1f) and Li(3c), respectively. These are the environments considered in ref 26. Figure 13b illustrates the second configuration, in which no Li ions lie above a trimer: instead they are edge-and corner-sharing, resulting in a single environment Li(1e1c) assuming a random arrangement of Li relative to the V layers. If a second V layer is placed above the Li layer, further possible Li environments occur. Figure 13c corresponds to the arrangement shown in Figure 13a, but incorporating a second V layer placed so that one Li now shares faces with two trimers, while the other two Li ions are corner-sharing with six trimers, resulting in a single Li(2f) and two Li(6c) environments. The probability that this arrangement occurs is 1/12 [derived as  $C_3^1/C_6^1 C_6^1$ , where  $C_n^1$  denotes a binomial coefficient]. Figure 13d shows a second stacking sequence formed from that shown in Figure 13a, but here arranged such that the trimers stack above Li ions that do not share faces with the trimers in the other V layer. This arrangement occurs with a probability of 1/6 [ $(C_3^1 C_2^1)/(C_6^1 C_6^1)$ ] and results in two Li(1f, 3c) and a single Li(6c) environment. The stacking in Figure 13e with probability 1/2 [ $(C_6^1 C_3^1)/(C_6^1 C_6^1)$ ] is formed from the stacking sequences shown in Figures 13a and b, and hence face-, edge-, and corner-sharing environments result, namely, a single Li(1e1c,1f) and two Li(1e1c,3c). A final arrangement with a probability of 1/4

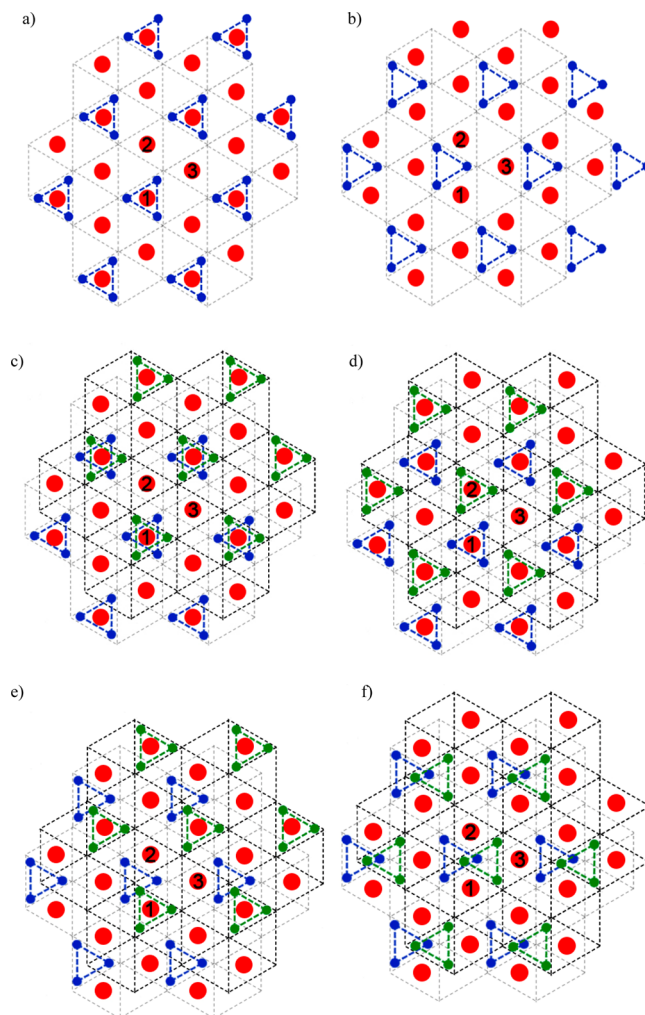


**Figure 13.** Projections along the [001] direction shown to demonstrate the different stacking arrangements of the vanadium layers and the resulting Li configurations. The gray hexagonal lattice and blue trimers denote the V positions in the first layer. The dark hexagonal lattice and the green trimers represent the second V layer. Red dots denote the Li positions between the two V layers. The three numbers indicate the different Li environments. Panels (a) and (b) illustrate the two possible stacking sequences of a single vanadium layer and the next Li layer. Only (a) results in face sharing of lithium with the vanadium trimers. A second vanadium layer can then be stacked on either (a) or (b) to create stacking sequences (c)–(f).

$[(C_3^1 C_3^1)/(C_6^1 C_6^1)]$  may be formed from stacking based in Figure 13b only, resulting only in Li ions that edge- and corner-share with trimers, namely, three Li(1e1c, 1e1c) environments. The probabilities with which each of these different environments occur are summarized in Table 4.

The initial PDF structural refinements identified 27 stacking sequences from among the total of 36 originally tested with  $R_w$  values of less than or equal to 20.7% (Supporting Information, Figure S7). Eighteen of these (with  $R_w$  values of  $\leq 20.2\%$ ) all contain stacking sequences comprising only arrangements D, E, and F but with different stacking orders. The structure employed as the initial model for PDF structural refinement was straightforwardly chosen on the basis of its lowest  $R_w$ , but it is noted that the stacking sequence of vanadium layers in this structure does not differ significantly from those occurring within the other 17 members of this group. The remaining 9 (with  $R_w$  values around 20.5%) only contain arrangement E,

Table 4. Different Li Configurations Generated by the 4 Stacking Sequences C–F, Shown in Figure 11<sup>a</sup>

sequence	Li environment						probability
C	Li(2f) Li(6c)						1/36 2/36
D	Li(1f,3c) Li(6c)						4/36 2/36
E	Li(1e1c, 1f) Li(1e1c, 3c)						6/36 12/36
F	Li(1e1c, 1e1c)						9/36
Li environment							
	Li(2f)	Li(6c)	Li(1f,3c)	Li(1e1c, 1f)	Li(1e1c, 3c)	Li(1e1c, 1e1c)	
probability	1/36	4/36	4/36	6/36	12/36	9/36	

<sup>a</sup>The probability that each configuration occurs, assuming a random stacking of vanadium layers, is shown for each stacking sequence and then for each configuration.

while the remaining nine stacking sequences with  $R_w$  higher than 22.2% comprise solely arrangement C, and therefore contain trimers stacked directly on top of each other with Li ions sandwiched in the intervening layer. Arrangement C is likely to be the least favorable arrangement on energetic grounds as a consequence of the large electrostatic repulsions between the Li and V cations, consistent with the lack of clear-cut evidence for this stacking sequence in the PDF analyses. However, regardless of the differences in V local structure associated with the variations in stacking sequences just discussed, the superlattice reflections of all models will appear at essentially the same  $2\theta$  angle, albeit with slightly different relative intensities. Removing the environments generated by sequence C from our analysis, only three Li environments with probabilities of greater than or equal to 16.6% remain (note that the Li environments generated by arrangement C contribute only 8.3% of the total number of Li ions, assuming random stacking). We tentatively assign the environment Li(1e1c, 1e1c) to the resonance at  $-1.4$  ppm since this configuration occurs alone in stacking arrangement F, which is in agreement with the proximity of Li sites in the 2D NMR experiment, and also has a higher probability of 25%. The other major environments Li(1e1c,1f) and Li(1e1c,3c) occur with probabilities of 16.6 and 33% and are assigned to the resonances at 1.7 and  $-2.9$  ppm, respectively, on the basis of the weaker intensity of the resonance at 1.7 ppm and the fact that the former environment shares faces with a trimer, likely leading to a shift that will be more distinct from the other two. Both of these environments originate in configuration E, consistent with the cross-peak observed between the 1.7 and  $-2.9$  ppm peaks in the 2D NMR spectrum of LiVO<sub>2</sub> indicative of the spatial proximity of the two originating environments. The other environment found in sequence D that occurs with significant probability (11.1%) is Li(1f,3c). This should give rise to a shift similar to that for Li(1e1c, 1f), and it is likely that the resonances from these two environments overlap, resulting in the higher intensity of this apparently single resonance. The sum of the probabilities for Li(1f, 3c) and Li(1e1c, 1f) (environments) amounts to  $10/36 = 27.8\%$  assuming random stacking of the layers. This calculated intensity is higher than observed, again suggesting non-random stacking, and that face-sharing environments are energetically disfavored.

The relative intensities of <sup>6</sup>Li signals arising from the three components do not change significantly on increase of Li content (Figure 5), save for a small decrease in the intensity of the Li(1e1c, 1e1c) resonance at 1.4 ppm and a considerable overall broadening of the <sup>6</sup>Li NMR spectra. No distinct

resonance is observed that might be assigned to Li ions residing in the V<sup>2+</sup> layers, the presence of which has been suggested by previous neutron diffraction.<sup>7</sup> Li substitution into the V layers of Li<sub>1+x</sub>V<sub>1-x</sub>O<sub>2</sub> results in an increase in V oxidation state in a notional Li<sub>1+x</sub>V<sup>4+</sup><sub>2x</sub>V<sup>3+</sup><sub>1-3x</sub>O<sub>2</sub> stoichiometry. The present PDF results show that the trimer motif is still present even in materials with the highest Li contents, despite the fact that such materials must contain substantial concentrations of V<sup>4+</sup> cations (e.g., the average vanadium oxidation state at  $x = 0.1$  is V<sup>3.29+</sup>). One possibility is that V<sup>3+</sup>–V<sup>3+</sup>–V<sup>3+</sup> trimers may be replaced by LiV<sup>4+</sup><sub>2</sub> clusters, minimizing the disruption of the trimers at even the highest Li substitution levels. Such LiV<sup>4+</sup><sub>2</sub> clusters should result in V<sup>4+</sup>–V<sup>4+</sup> contacts. However such contacts will be present at very low concentrations and will be difficult to detect in the PDF patterns. It is nevertheless surprising that no distinct resonances originating from Li nearby V<sup>4+</sup> cations (either in the V or Li layers) are observed, given that distinct resonances are observed for the Li-deficient Li<sub>1-x</sub>VO<sub>2</sub> materials, which also contain V<sup>4+</sup> cations. Possible explanations for this include mobility of the Li<sup>+</sup> ions, consistent with the much weaker Li correlations seen in the 2D spectrum of Li<sub>1.07</sub>V<sub>0.93</sub>O<sub>2</sub> and/or mobility of the electrons, resulting in a partial or complete averaging of the effective V oxidation state. Both phenomena might result in the broadening of the spectra that is observed experimentally. Magnetic coupling between the V<sup>4+</sup> d<sup>1</sup> ions to produce a singlet dimer is certainly also possible. Low temperature NMR spectroscopy to explore such phenomena in greater detail is in progress. The proposed increase in Li<sup>+</sup> mobility in the Li-excess phases is consistent with their improved electrochemical performance.

The NMR spectra of the materials obtained at the beginning of the discharge support the proposal that the first two processes observed in the electrochemistry involve SEI formation and electrolyte decomposition, as no change in the NMR signal is seen. However, the “60 mA h g<sup>-1</sup>” sample was obtained following discharge to the point where the intermediate phase was identified by diffraction,<sup>7</sup> and yet no new signal was observed. This is most likely due to the extreme sensitivity of this sample to both air and moisture, the exposure to which most likely occurred during the NMR experiments, since the NMR rotors are not completely airtight. Moreover, the NMR experiments were performed with nitrogen spinning gas, and the intermediate phase has been observed to readily react with N<sub>2</sub> to form Li<sub>3</sub>N. Experiments are in progress to explore this further. Two distinct resonances are observed in the “125 mA h g<sup>-1</sup>” sample from Li<sub>1.07</sub>V<sub>0.93</sub>O<sub>2</sub> and Li<sub>2+x</sub>V<sub>1-x</sub>O<sub>2</sub>, the Li<sub>2</sub>VO<sub>2</sub> resonance being observed at this stage of discharge.

## CONCLUSIONS

PDF analysis of the synchrotron X-ray diffraction patterns for a series of  $\text{Li}_{1+x}\text{V}_{1-x}\text{O}_2$  samples provides clear evidence for the formation of  $\text{V}^{3+}-\text{V}^{3+}-\text{V}^{3+}$  trimers even in the most lithiated compound studied here ( $x = 0.1$ ). V–V correlations at 2.54(2) and 3.00(2) Å (Table 3) are observed, which may be regarded as characteristic signatures of trimer formation given that they correspond to V–V distances within and between the trimers, respectively. Such V–V distances correspond to a displacement of the V atoms by 0.17(2) Å from the normal sites of the undistorted  $\alpha$ - $\text{NaFeO}_2$  lattice. A structural model was derived which captured the local distortions of both the V and the O atoms. Refinements showed that stacking sequences of the V layers favored arrangements with fewer Li ions located directly above or below (i.e., face-sharing) the V trimers. The NMR spectra of these samples confirmed that the V display a strong magnetic ordering to form a diamagnetic  $S = 0$  spin state, again consistent with previous theories of trimer formation.<sup>10</sup> Three dominant  ${}^6\text{Li}$  signals are observed that are assigned to the different environment resulting from the stacking of the trimer-containing layers along the hexagonal *c*-axis, the results again suggesting that local arrangements minimizing the number of Li ions face-sharing with trimers are favored. The more lithiated samples appear to contain considerable disorder, which we believe may contribute to the more favorable electrochemistry of these samples.  $\text{Li}_2\text{VO}_2$  is clearly observed by NMR in the electrochemically lithiated samples, but the intermediate phase was not seen, possibly because of the sensitivity of this sample to trace amounts of moisture. Solid state hybrid DFT calculations were used to rationalize the origin of the negative Li hyperfine shift seen for  $\text{Li}_2\text{VO}_2$ , providing additional insights into electronic structure, magnetic coupling, and magnetostructural distortions.

## ASSOCIATED CONTENT

### Supporting Information

Details of DFT calculations, relationship between the  $\alpha$ - $\text{NaFeO}_2$  structure and the superstructure, simulated electron and X-ray diffraction patterns, further PDF analyses and NMR spectra, electrochemical profile, distribution of PDF *Rw*-factors across all refined models, structures obtained from PDF refinements, computed electronic structure of  $\text{Li}_2\text{VO}_2$ . This material is available free of charge via the Internet at <http://pubs.acs.org>.

## AUTHOR INFORMATION

### Corresponding Author

\*E-mail: cpg27@cam.ac.uk

### Author Contributions

<sup>#</sup>Authors contributed equally to this manuscript.

### Notes

The authors declare no competing financial interest.

## ACKNOWLEDGMENTS

We wish to thank EPSRC for funding via the SUPERGEN consortium and via the “nanoionics” program grant. Research was carried out (in whole or in part) on the NANO computer cluster at the Center for Functional Nanomaterials, Brookhaven National Laboratory, which is supported by the U.S. Department of Energy, Office of Basic Energy Sciences, under Contract No. DE-AC02-98CH10886. We thank Prof. S. Islam,

Dr. P. Panchmatia, and Dr. E. Castillo-Martínez for helpful discussions.

## REFERENCES

- (1) Mizushima, K.; Jones, P. C.; Wiseman, P. J.; Goodenough, J. B. *Mater. Res. Bull.* **1980**, *15*, 783–789.
- (2) Thackeray, M. M.; Depicciotto, L. A.; David, W. I. F.; Bruce, P. G.; Goodenough, J. B. *J. Solid State Chem.* **1987**, *67*, 285–290.
- (3) Depicciotto, L. A.; Thackeray, M. M.; Pistoia, G. *Solid State Ionics* **1988**, *28*, 1364–1370.
- (4) Dahn, J. R.; Vonsacken, U.; Juzkow, M. W.; Aljanaby, H. *J. Electrochem. Soc.* **1991**, *138*, 2207–2211.
- (5) Choi, N. S.; Kim, J. S.; Yin, R. Z.; Kim, S. S. *Mater. Chem. Phys.* **2009**, *116*, 603–606.
- (6) Song, J. H. *J. Power Sources* **2010**, *195*, 6157–6161.
- (7) Armstrong, A. R.; Lyness, C.; Panchmatia, P. M.; Islam, M. S.; Bruce, P. G. *Nat. Mater.* **2011**, *10*, 223–229.
- (8) Depicciotto, L. A.; Thackeray, M. M.; David, W. I. F.; Bruce, P. G.; Goodenough, J. B. *Mater. Res. Bull.* **1984**, *19*, 1497–1506.
- (9) Du, F.; Li, A.; Liu, D.; Zhan, S.; Hu, F.; Wang, C.; Chen, Y.; Feng, S.; Chen, G. *J. Magn. Magn. Mater.* **2009**, *321*, 1975–1979.
- (10) Goodenough, J. B.; Dutta, G.; Manthiram, A. *Phys. Rev. B* **1991**, *43*, 10170–10178.
- (11) Pen, H. F.; vandenBrink, J.; Khomskii, D. I.; Sawatzky, G. A. *Phys. Rev. Lett.* **1997**, *78*, 1323–1326.
- (12) Yoshitake, J.; Motome, Y. *J. Phys. Soc. Jpn.* **2011**, *80*, 073711.
- (13) Ezhev, S. Y.; Anisimov, V. I.; Pen, H. F.; Khomskii, D. I.; Sawatzky, G. A. *Europhys. Lett.* **1998**, *44*, 491–497.
- (14) Kobayashi, K.; Kosuge, K.; Kachi, S. *Mater. Res. Bull.* **1969**, *4*, 95–106.
- (15) Onoda, M.; Naka, T.; Nagasawa, H. *J. Phys. Soc. Jpn.* **1991**, *60*, 2550–2553.
- (16) Tian, W.; Chisholm, M. F.; Khalifah, P. G.; Jin, R.; Sales, B. C.; Nagler, S. E.; Mandrus, D. *Mater. Res. Bull.* **2004**, *39*, 1319–1328.
- (17) Yamakawa, N.; Jiang, M.; Key, B.; Grey, C. P. *J. Am. Chem. Soc.* **2009**, *131*, 10525–10536.
- (18) Key, B.; Morcrette, M.; Tarascon, J.-M.; Grey, C. P. *J. Am. Chem. Soc.* **2011**, *133*, 503–512.
- (19) Breger, J.; Dupre, N.; Chupas, P. J.; Lee, P. L.; Proffen, T.; Parise, J. B.; Grey, C. P. *J. Am. Chem. Soc.* **2005**, *127*, 7529–7537.
- (20) Armstrong, A. R.; Dupre, N.; Paterson, A. J.; Grey, C. P.; Bruce, P. G. *Chem. Mater.* **2004**, *16*, 3106–3118.
- (21) Bowden, W.; Grey, C. P.; Hackney, S.; Wang, F.; Paik, Y.; Iltchev, N.; Sirotna, R. *J. Power Sources* **2006**, *153*, 265–273.
- (22) Cabana, J.; Shirakawa, J.; Chen, G. Y.; Richardson, T. J.; Grey, C. P. *Chem. Mater.* **2010**, *22*, 1249–1262.
- (23) Grey, C. P.; Dupre, N. *Chem. Rev.* **2004**, *104*, 4493–4512.
- (24) Tanaka, T.; Kawasaki, Y.; Endou, S.; Kimura, S.; Ideta, Y.; Kishimoto, Y.; Ohno, T.; Katayama, N.; Nohara, M.; Takagi, H. *J. Phys. Soc. Jpn.* **2009**, *78*, 054709.
- (25) Kikuchi, J.; Kambe, S.; Yasuoka, H.; Ueda, Y.; Tomimoto, K.; Akimitsu, J. *J. Phys. Soc. Jpn.* **1991**, *60*, 3620–3624.
- (26) Takao, K.; Onoda, M. *J. Phys.: Condens. Matter* **2010**, *22*, 116003.
- (27) Lee, Y. K.; Kurur, N. D.; Helmle, M.; Johannessen, O. G.; Nielsen, N. C.; Levitt, M. H. *Chem. Phys. Lett.* **1995**, *242*, 304–309.
- (28) Hohwy, M.; Jakobsen, H. J.; Eden, M.; Levitt, M. H.; Nielsen, N. C. *J. Chem. Phys.* **1998**, *108*, 2686–2694.
- (29) Egami, T.; Billinge, S. J. L. In *Pergamon Materials Series*; Cahn, R. W., Ed.; Elsevier: Amsterdam, The Netherlands, 2003; Vol. 7.
- (30) Hammersley, A. *FIT2D*, V9.129 reference manual V3.1, ESRF internal report 98HA01T; European Synchrotron Radiation Facility (ESRF): Grenoble, France, 1998.
- (31) Qiu, X.; Thompson, J. W.; Billinge, S. L. J. *J. Appl. Crystallogr.* **2004**, *37*, 678.
- (32) Chupas, P. J.; Qui, J. C.; Hanson, P. L.; Grey, C. P.; Billinge, S. L. J. *J. Appl. Crystallogr.* **2003**, *36*, 1342–1347.

- (33) Farrow, C. L.; Juhas, P.; Lui, J. W.; Bryndin, E. S.; Bozin, J.; Bloch, T.; Proffen, T.; Billinge, S. J. L. *J. Phys.: Condens. Matter* **2007**, *19*, 335219.
- (34) Rodriguez-Carvajal, J. *Phys. B* **1993**, *192*, 55–69.
- (35) Dovesi, R.; Saunders, V. R.; Roetti, C.; Orlando, R.; Zicovich-Wilson, C. M.; Pascale, F.; Civarelli, B.; Doll, K.; Harrison, N. M.; Bush, I. J.; D'Arco, P.; Llunell, M. *CRYSTAL09 User's Manual*; University of Torino: Torino, Italy, 2009.
- (36) Muscat, J.; Wander, A.; Harrison, N. M. *Chem. Phys. Lett.* **2001**, *342*, 397–401.
- (37) Cora, F.; Alfredsson, M.; Mallia, G.; Middlemiss, D. S.; Mackrodt, W. C.; Dovesi, R.; Orlando, R. In *Principles and Applications of Density Functional Theory in Inorganic Chemistry II*; Kaltsos, N., McGrady, J. E., Eds.; Springer: Berlin, Germany, 2004; Vol. 113, pp 171–232.
- (38) Moreira, I. D. R.; Illas, F.; Martin, R. L. *Phys. Rev. B* **2002**, *65*, 155102.
- (39) Feng, X. B.; Harrison, N. M. *Phys. Rev. B* **2004**, *70*, 092402.
- (40) Middlemiss, D. S.; Lawton, L. M.; Wilson, C. C. *J. Phys.: Condens. Matter* **2008**, *20*, 355231.
- (41) Kim, J.; Middlemiss, D. S.; Chernova, N. A.; Zhu, B. Y. X.; Masquelier, C.; Grey, C. P. *J. Am. Chem. Soc.* **2010**, *132*, 16825–16840.
- (42) Carlier, D.; Menetrier, M.; Grey, C. P.; Delmas, C.; Ceder, G. *Phys. Rev. B* **2003**, *67*, 174103.
- (43) Mabbs, F. E.; Machin, D. J. *Magnetism and Transition Metal Complexes*; Dover Publications Inc.: Mineola, NY, 2008.
- (44) Grey, C. P.; Lee, Y. J. *Solid State Sci.* **2003**, *5*, 883–894.